p-Type β-Ga2O3 Homoepitaxial Films with Superior Electrical Transport Properties

Zeyu Chi, Corinne Sartel, Vincent Sallet, Bruno Berini, Yves Dumont, Yunlin Zheng, Leonid Chernyak, Miquel Vellvehí, Amador Pérez-tomás, Ekaterine Chikoidze

To cite this version:

Zeyu Chi, Corinne Sartel, Vincent Sallet, Bruno Berini, Yves Dumont, et al.. p-Type β-Ga2O3 Homoepitaxial Films with Superior Electrical Transport Properties. Advanced Electronic Materials, 2025, ⟨10.1002/aelm.202500190⟩. ⟨hal-05230264⟩

HAL Id: hal-05230264
https://hal.science/hal-05230264v1

Submitted on 29 Aug 2025

RESEARCH ARTICLE

ADVANCED ELECTRONIC MATERIALS
Open Access
www.advelectronicmat.de

p-Type β-Ga_2O_3 Homoepitaxial Films with Superior Electrical Transport Properties

*Zeyu Chi, Corinne Sartel, Vincent Sallet, Bruno Berini, Yves Dumont, Yunlin Zheng, Leonid Chernyak, Miquel Vellvehí, Amador Pérez-Tomás, and Ekaterine Chikoidze**

This work reports high structural quality and exceptional electrical transport properties of homoepitaxial β-Ga_2O_3 thin films grown by Metal–Organic Chemical Vapor Deposition (MOCVD) on (010)- and (–201)-oriented substrates. (010) β-Ga_2O_3 samples exhibit mobility of up to 69.4 cm^2 (V·s)$^{-1}$ and stable hole concentrations $\approx 2.4 \times 10^{17}$ cm^{-3} from 370 to 700 K. Structural and morphological studies, including XRD, AFM, and STEM, confirm high epitaxial quality, absence of extended defects and minimal strain. (–201) β-Ga_2O_3 layer, which is simultaneously grown, exhibits typical *p*-Ga_2O_3 behavior with observed deep level defects. The hole mobility ranging from 26 to 36 cm^2 V^{-1}·s^{-1} is measured between 420 and 700 K. Comparison of (010) and (–201) orientations reveals distinct anisotropic electrical properties. The findings emphasize the free motion of holes in β-Ga_2O_3 and the critical role of crystallographic orientation.

1. Introduction

Over the past decade, Gallium Oxide (Ga_2O_3) has attracted significant interest for the next-generation of power electronics and optoelectronics. Ga_2O_3 exhibits a collection of outstanding electronic properties such as ultra-wide bandgap (UWBG) of 4.6–4.9 eV, high breakdown electrical field larger than 8 MV cm^{-1},[1,2] availability of 6-inch wafers, excellent control of *n*-type doping with concentrations ranging from 10^{16} to 10^{20} cm^{-3},[3–7] and room-temperature electron mobility exceeding 200 cm^2 (V·s)$^{-1}$.[8] Additionally, electronic devices such as field effect transistors,[9,10] Schottky barrier diodes,[11] *p*-NiO/*n*-Ga_2O_3 heterojunction diodes,[12,13] and 2D transistors[14] showed the great potential of this material for advancements in power electronics. Besides, β-Ga_2O_3 has shown significant promise in solar-blind ultraviolet sensors, especially in the UVC region, due to both its UWBG and superior radiation hardness compared to GaN.[15–19] Solar-blind photodetectors are insensitive to infrared, visible, and near-UV light, but respond to ultraviolet radiation with wavelengths below 300 nm, which is completely absorbed by the atmospheric ozone layer, enabling selective detection of UVC sources, leading to a low false-alarm rate.[17,20–22]

To realize the full functionality of any emerging electronic technology based on UWBG semiconductors, both *n*- and *p*-type conductivity (i.e., bipolarity) should be attained. Till recently, a drawback with bipolar Ga_2O_3 technology was related to the absence of robust homoepitaxial *p*-type layers possessing high conductivity at room temperature. This obstacle has led to heterostructures mainly using polycrystalline *p*-NiO as *p*-type oxides.[12,23–25] Several publications have demonstrated the native defect-related hole conductivity in β-Ga_2O_3 films grown on sapphire. The origin of the free holes in undoped *p*-Ga_2O_3 was attributed to the Ga vacancies with deep ionization energy $E_i = 1.12$ eV[26,27] and levels associated with native defects.[28–30] Efficient *p*-type doping of β-Ga_2O_3 layers with Zn,[1,28,31] N,[32] and P (by implantation) was later reported.[33,34] Very recently, β-Ga_2O_3-based *p*-*n* homojunctions grown on *c*-sapphire[35–38] and Si/SiO_2[39] substrates have been demonstrated.

It is worth emphasizing that significant advancements have been made in the growth of high quality *n*-type homoepitaxial β-Ga_2O_3 thin-films on substrates with (–201), (100), (010), and (001) crystallographic orientations using MOCVD,[5,40–42] MOVPE,[43–45] LPCVD,[46] HVPE,[47,48] MBE.[49] However, demonstrations of Ga_2O_3 homo *p*-*n* junctions are still handful. To efficiently address the urgent demand for *p*-*n*

Z. Chi, C. Sartel, V. Sallet, B. Berini, Y. Dumont, E. Chikoidze
Groupe d'Etude de la Matière Condensée (GEMaC)
CNRS
Université Paris-Saclay
Université de Versailles St-Quentin en Yvelines
45 Av. des Etats-Unis, Versailles 78035 Cedex, France
E-mail: ekaterine.chikoidze@uvsq.fr

Y. Zheng
Institut des Nano Sciences de Paris (INSP)
CNRS UMR7588
Sorbonne Université
4 place Jussieu, Paris 75252, France

L. Chernyak
Department of Physics
University of Central Florida
Orlando, FL 32816, USA

M. Vellvehí, A. Pérez-Tomás
Institute of Microelectronics of Barcelona (IMB-CNM-CSIC)
C/ dels Til.lers s/n, Campus UAB, Bellaterra, Barcelona 08193, Spain

The ORCID identification number(s) for the author(s) of this article can be found under https://doi.org/10.1002/aelm.202500190

DOI: 10.1002/aelm.202500190

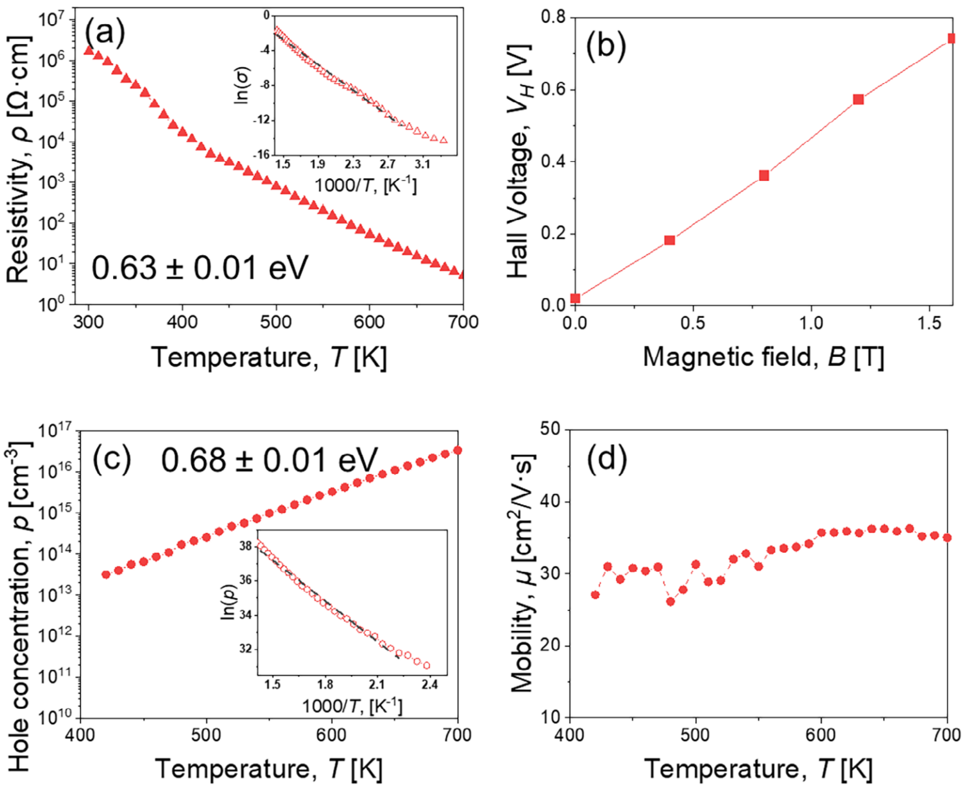

Figure 1. Electrical transport properties of homoepitaxially grown (–201) β-Ga_2O_3 sample: a) Temperature-dependent resistivity b) Hall voltage as a function of applied magnetic field at 500 K. c) Hall hole concentration and d) Hall hole mobilities versus temperature. Inset in (a) and (c): Arrhenius plots for conductivity and hole concentration, for the determination of activation energies for conductivity and carrier concentration, respectively.

homojunction realization, the first necessary step is to grow high-quality p-type β-Ga_2O_3 layers with hole conductivity measurable at or near room temperature.

This work demonstrates high structural quality undoped p-type β-Ga_2O_3 epitaxial layers with distinct electrical transport properties grown on (–201)- and (010)-oriented gallium oxide substrates. Remarkable high hole concentration and mobility from 370 K for (010) β-Ga_2O_3 films opens a way for homojunction fabrication, simultaneously revealing the nature of electrical anisotropy related to crystallographic orientations. These findings are crucial for the realization of p-n homojunctions – essential building blocks for a wide range of power electronic and optoelectronic devices.

2. Electrical Transport Properties

β-Ga_2O_3 epilayers were simultaneously grown at 775 °C on (010)- and (–201)-oriented Fe-doped insulating Ga_2O_3 substrates by Metal–Organic Chemical Vapor Deposition (MOCVD). The electrical transport properties were measured in a Van der Pauw configuration to determine the resistivity, carrier type, density and mobility. The electrical contacts were prepared using silver paste with in situ annealing at the four corners of 1×1 cm^2 square-shaped sample.

The β-Ga_2O_3 (–201) sample showed a typical semiconductor-like behavior with high hole activation energy (i.e., exhibiting partial ionization). **Figure** 1a shows the temperature-dependent electrical resistivity between 300 and 700 K with $\rho \approx 2 \times 10^6$ Ω·cm at room temperature (the activation energy for electrical conductivity was determined at 0.63 eV (Inset in Figure 1a). As shown in Figure 1b, positive Hall voltage increases with increasing applied magnetic field, indicating the p-type conductivity.

The hole concentration decreased from 3.4×10^{16} to 3.1×10^{13} cm^{-3} (Figure 1c) for temperatures ranging from 700 to 420 K with an activation energy of 0.68 eV. The Hall hole mobility varies slightly between 36 and 26 cm^2 (V·s)$^{-1}$ (Figure 1d). Similar temperature dependence of resistivity and hole concentration have been previously reported for highly (E_a = 1.2 eV) and less (E_a ≈0.6 eV) compensated β-Ga_2O_3//Al_2O_3 thin films.[26,29,30] In either case, the origin of holes was associated to V_{Ga} defects. The homoepitaxial layer exhibits ≈3 times higher mobility as compared to β-Ga_2O_3//Al_2O_3 ($\mu \approx 10$ cm^2 (V·s)$^{-1}$ at 850 K),[29] which can be attributed to its significantly improved structural quality.

Figure 2 presents the electrical transport properties of the simultaneously deposited (010) β-Ga_2O_3 thin layer, as characterized in a Van der Pauw configuration in the temperature range from 370 to 700 K. This layer shows a totally different electrical behavior. As shown in Figure 2a, the resistivity increases slightly from 0.33 to 0.5 Ω·cm with temperature. Below ≈360 K, slight electrical contact degradation has been observed, thus room temperature resistivity value is extrapolated from a linear fit of the slope, as 0.28 Ω·cm. The positive increase in Hall voltage (V_H) with applied magnetic field (B) at 500 K reveals the p-type nature of electrical conductivity (Figure 2b).[26] The hole concentration

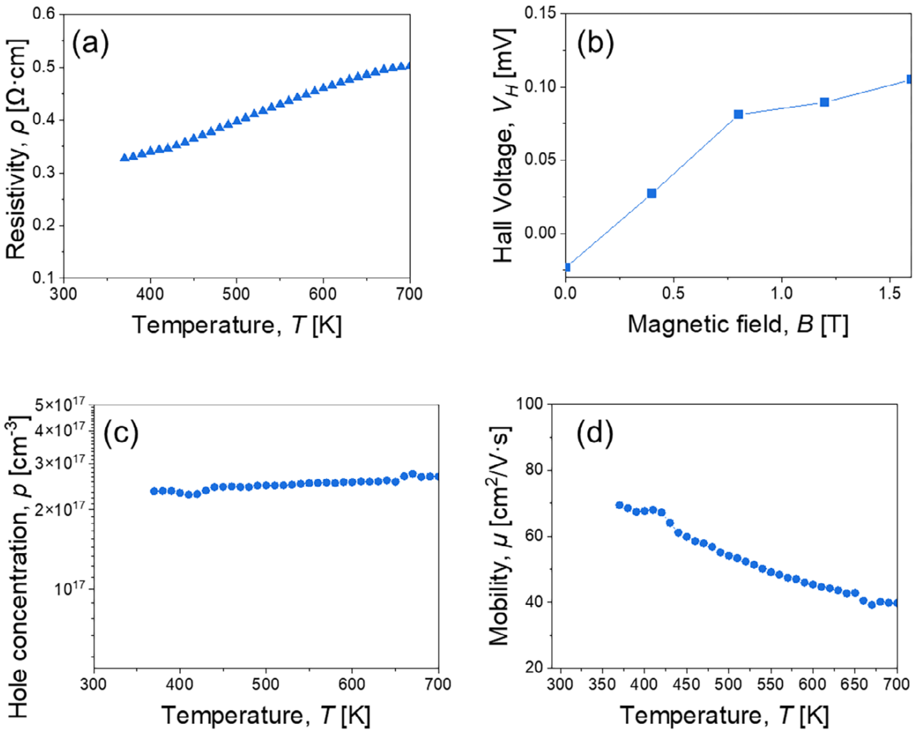

Figure 2. Electrical transport properties of homoepitaxially-grown β-Ga_2O_3 (010) sample: a) Temperature-dependent resistivity b) Hall voltage as a function of applied magnetic field at 500 K. c) Hall hole concentration and d) Hall hole mobilities versus temperature.

remains nearly invariant at ≈2.4 × 10^{17} cm^{-3} across the measured temperature range (Figure 2c), suggesting that the density of thermally activated carriers does not significantly change above room temperature. As shown in Figure 2d, the Hall mobility shows a decrease from 69.4 to 39.8 cm^2 $(V\cdot s)^{-1}$ with increasing temperature from 370 to 700 K. In β-Ga_2O_3, optical phonon (OP), acoustic deformation potential (ADP), ionized impurity (II), and neutral impurity (NI) scattering mechanisms are generally considered when analyzing carrier mobility, each with different temperature-dependent behaviors.[5,50–52] As given in reference,[52] OP scattering has a major impact at room and elevated temperatures and it follows $\mu_{PO} \approx 1/T$ dependence. At lower temperatures, the carrier mobility is limited by impurities, following $\mu_{II} \approx T^{3/2}$. At the same time, NI and ADP scatterings have minor influence on mobility. Our experimental mobility dependence on T qualitatively agrees with the previously reported optical phonon scattering in β-Ga_2O_3.[5,52] Moreover, Ma et. al.[51] demonstrated a significant increase in ADP-related mobility after N doping. The electrical conductivity shows temporal (we have performed measurements within 5 and 14 months intervals) and temperature (cycling up to 750 K) stability. While samples with (–201) crystallographic orientations show usual behavior of semiconducting material, the extraordinary properties observed for (010) Ga_2O_3 merit detailed structural studies, discussed in the paragraph below.

3. Structural Properties

To understand the origin of superior electrical properties for (010) β-Ga_2O_3 thin films, detailed structural, chemical, and morphological studies were carried out. The techniques such as X-ray diffraction (XRD), atomic force microscopy (AFM), and scanning transmission electron microscopy (STEM) were employed.

X-ray reflectivity (XRR) indicates a surface roughness (σ) of 2.0 nm (**Figure 3a**), versus 0.3 nm for the as-received substrate evaluated prior to growth. As was expected, the $\theta/2\theta$ scan displays only the 020 reflection with no additional reflections, indicating complete homoepitaxy and high crystalline quality of the film (Figure 3b). The rocking curve of the reflection shows no notable difference from the substrate, with a full width at half maximum (FWHM) of 0.013° for the (010) lattice planes, which is very close to the value of 0.010° for the substrate (see inset 3 (b)). The small FWHM value of several tens of arcsec indicates the high crystallinity of thin films deposited on β-Ga_2O_3 substrates.

Surface atomic force microscopy (AFM) images taken for three different scales ranging from 200 nm to 1 µm, along with surface root mean square (RMS) roughness, of homoepitaxial β-Ga_2O_3 (010) film are shown in Figure 3c–e. The grooves, elongated along [001] direction (cf. Figure 11c–e), were also observed in β-Ga_2O_3 films grown by grown by MBE,[49,53] MOCVD,[5] LPCVD.[46] The RMS of the surface depends on the growth rate[54] and temperature,[42,53] and can also be reduced by such pretreatment as Ar annealing.[41] In reference,[54] the surface roughness decreased from 5.87 to 0.62 nm for β-Ga_2O_3 films grown by MOCVD on (010) Ga_2O_3 substrates at 800–1000 °C, while the growth rate was reduced from 1.6 to 0.9 µm h^{-1}.

Figure 4 shows the Raman spectra recorded in 130–800 cm^{-1} range using 514.5 nm excitation for (010) β-Ga_2O_3 single crystal and homoepitaxially grown layers. All these samples exhibit

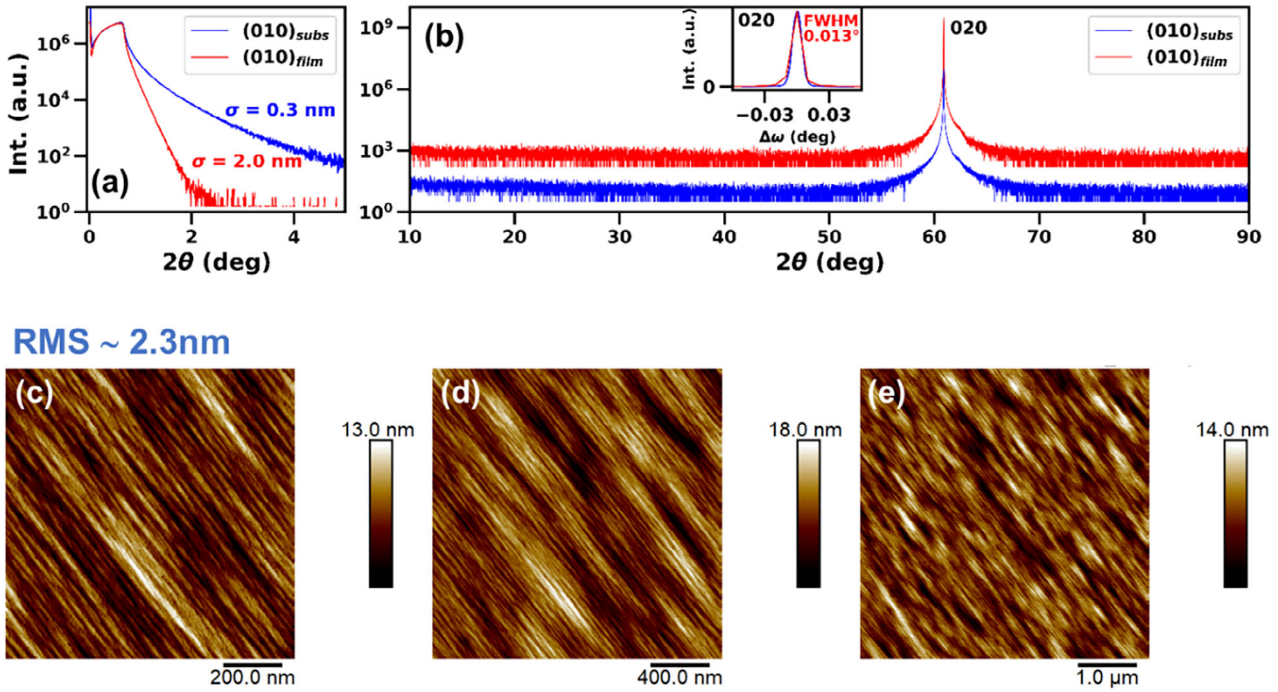

Figure 3. X-ray a) reflectivity and b) diffraction of homoepitaxial β-Ga_2O_3 (010) film (in red) compared with the scans of the substrates alone (in blue). σ in (a): surface roughness; inset in (b): rocking curves of 020 reflection where $\Delta\omega$ is the deviation from the angle of incidence of $\theta/2\theta$. c–e): Surface AFM images taken for three different scales, with an overall RMS of 2.3 nm.

the well-known active Raman phonon modes for (010) β-Ga_2O_3 at 170, 201, 321, 347, 417, 476, 631, 652, and 767 cm^{-1}.[55,56] The presence of strain in materials changes the phonon frequencies by compressing or stretching the lattice, leading to blue or redshifts.[57] In this work, for epilayers under test, there is almost no deviation in Raman shift relative to the substrate, indicating that the as-grown layers have strain and extended defect levels comparable with the single crystal substrates.[58] Different peak intensities in different orientations for individual phonon modes are attributed to the low symmetry of β-Ga_2O_3 and the effects of birefringence.[59]

High-angle annular dark field (HAADF) scanning transmission electron microscopy (STEM) images are shown in **Figure 5** and reveal that homoepitaxial growth occurred without the generation of extended defects or dislocations. In particular, no V-shape "sympetalous" defects, like those observed by,[44] have been found within the lamella. Such defects nucleate from nanotubes or dislocations in the substrate and further extend like inverted polycrystalline pyramids as the growth proceeds. The absence of extended defects in our sample suggests a low etch pit density in the supplied β-Ga_2O_3 (010) substrate and/or growth process that prevents propagation of surface defects through the epilayer. The interface with the substrate is hardly seen in Figure 5b, where only a very weak contrast can be distinguished at low magnification, indicating the successful homoepitaxy. Energy-dispersive X-ray spectroscopy (EDS) mappings carried out on the interface area did not reveal any contamination by extrinsic elements. Figure 5c with zoomed detail in the inset shows a HAADF image with high resolution taken in the epilayer. Noteworthy, a very similar image was taken in the substrate area (not shown here). The lattice of Ga atomic columns is clearly observed, and it fits perfectly with the Carine software simulation of the β-Ga_2O_3 crystal along the [001] zone axis, as illustrated in Figure 5d.

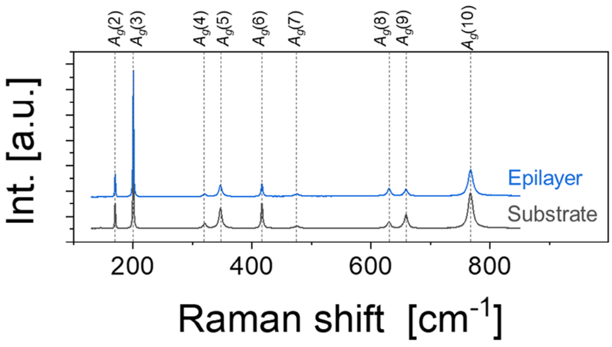

Figure 4. Raman spectra of homoepitaxial β-Ga_2O_3 (010) film (in blue) and substrate (in black).

Although no line or planar defects were found within the field of view in the lamella, point defects such as vacancies, interstitials, or complexes involving several of them, are expected in β-Ga_2O_3. Interestingly, from the HAADF-STEM intensities, Johnson et al. identified point defect complexes consisting of one Ga interstitial paired with two Ga vacancies, and directly correlated them with DFT calculations.[60] Shortly after, the same group investigated the structural properties of $(Al_{0.4}Ga_{0.6})_2O_3$ layers grown on β-Ga_2O_3 by atomic resolution STEM from [001] zone axis, and found out many cases where an additional Ga atomic

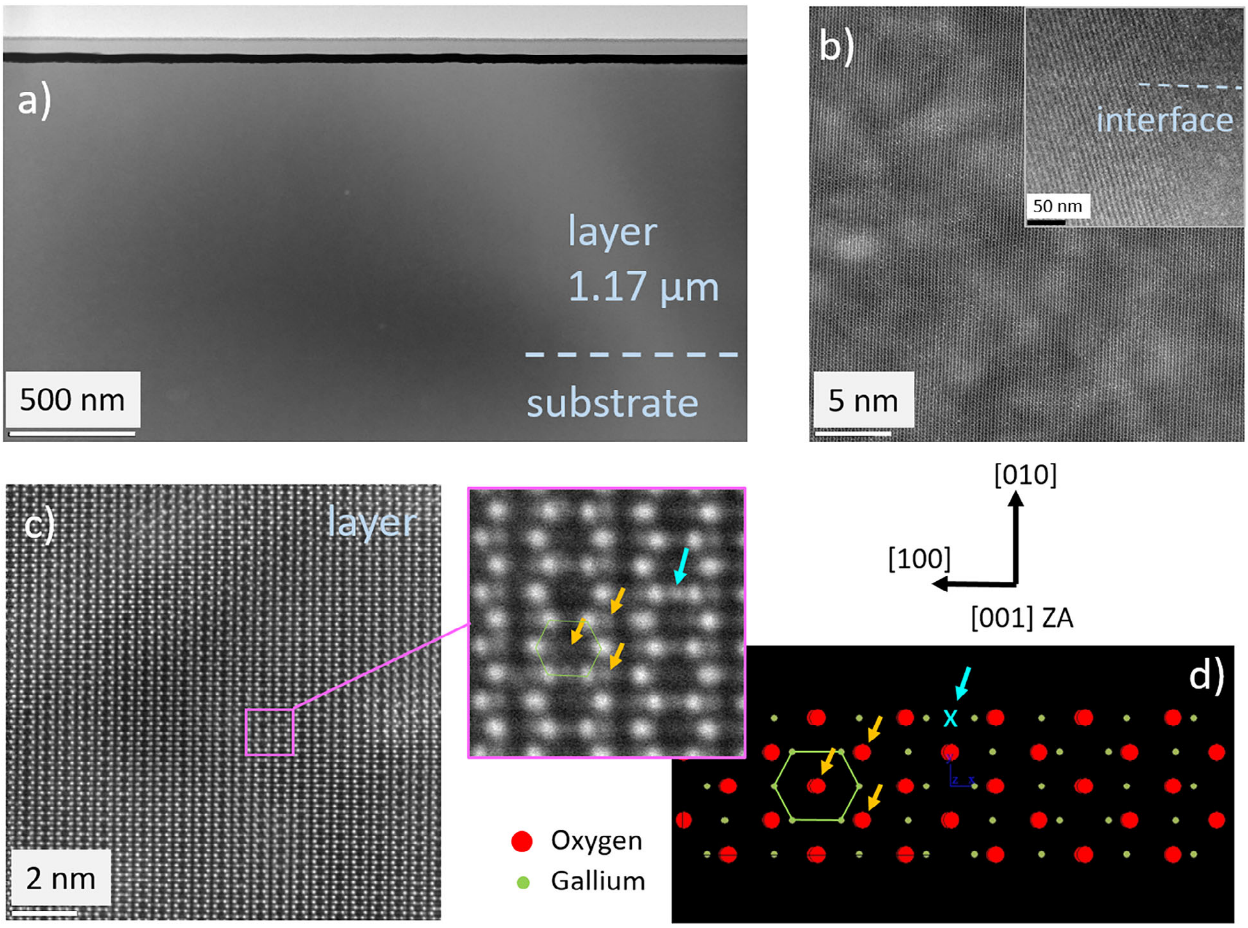

Figure 5. STEM analysis of a Ga_2O_3 epilayer grown on (010) Ga_2O_3 substrate, with [001] zone axis: a) low magnification HAADF image of the lamella covering layer and substrate regions, b) HAADF images at the interface, c) HAADF image with atomic scale resolution taken in the layer (in insert, detail showing additional bright contrasts indicated by arrows), and d) Carine simulation of the Ga (green atoms) and O (red atoms) lattices observed in β-Ga_2O_3 along [001] zone axis.

column (bright spot) is located in between two Ga1 positions.[61] These extra atomic columns, appearing as bright spots, were interpreted as interstitial Ga atoms, based on the reduced intensity of the adjacent Ga1 columns, which indicated associated divacancy–interstitial complexes.

In this work, STEM is also performed across [001] zone axis and we note the same occurrence of additional contrasts between two Ga1 atomic columns, as indicated by the blue arrow in the insert of Figure 5c, so that they are attributed to columns of interstitial Ga. This results in a significant density of short segments of three bright spots aligned along the [100] crystallographic direction in both epilayer and substrate areas. In addition, it appears that other additional spots with weaker brightness can be found at other positions where oxygen atomic columns are expected, as indicated by the orange arrows (Figure 5c). Their low intensity is explained by the HAADF-STEM conditions which are sensitive to the atomic number Z, therefore enhancing the gallium lattice at the expense of the oxygen lattice. Such observation was also reported by the reference.[62]

In conclusion, the (010) β-Ga_2O_3 sample exhibits a well-defined monophasic structure without extended defects. The interface is structurally stable and free of impurities.

4. Discussion

Homoepitaxial (–201) and (010) β-Ga_2O_3 thin films, which are free of extrinsic impurities and extended defects were successfully grown by MOCVD and demonstrated significantly different electrical transport properties. While *p*-type (–201) β-Ga_2O_3 layer showed a typical semi-insulating behavior, *p*-type (010) β-Ga_2O_3 thin film demonstrates hole concentration $\approx 2.4 \times 10^{17}$ cm^{-3}, which is almost invariant above room-temperature. This highlights the strong anisotropy in electronic properties in β-Ga_2O_3, which arises from different crystallographic orientations with distinct surface terminations, influencing, in turn, the thermodynamics of native defect formation. Indeed, (010) plane contains gallium atoms in tetrahedral (Ga1) and octahedral (Ga2) sites and oxygen atoms with a ratio of Ga:O = 2:3; the (–201) plane is exclusively composed of either Ga1, Ga2 or oxygen atoms, leading to different dangling bond density and surface energy.[30,63]

High hole concentration for (010) β-Ga_2O_3 thin film corroborate the recent key observation of this exact sample by electron beam-induced current (EBIC) technique.[64] Mainly, large minority carrier diffusion lengths (L_e) was measured to be ≈1 µm at

Table 1. Brief summary of parameters for several *p*-type oxide layers reported in the literature.

Materials	Structure	E_g [eV]	Substrate	Growth technique	p [cm^{-3}]	μ [cm^2 V^{-1}·s^{-1}]	Refs.
SnO	Tetragonal	–	Si/SiO$_2$	Sputtering	5.4×10^{18}	8.8	[74]
SnO	Tetragonal	≈2.7	Soda-lime glass	Sputtering	2.2×10^{17}	18.7	[75]
CuAlO$_2$	Delafossite	3.5	*c*-Al$_2$O$_3$	Solid-state reaction	1.3×10^{17}	10.4	[76]
LiGa$_5$O$_8$	Spinel cubic	5.36	*c*-Al$_2$O$_3$	Mist-CVD	1.9×10^{15}	20.1	[77]
Ba$_2$BiTaO$_6$	Perovskite	>4.5	MgO	PLD	10^{14}	30	[78]
Cu$_2$O	Cubic	2.17	MgO	PLD	1.7×10^{14}	90	[79]
Cu$_2$O	Cubic	–	Glass	Sputtering	1.0×10^{14}	256	[80]

room temperature, which is much longer than that for holes found in *n*-type β-Ga$_2$O$_3$ (L_h ≈100–300 nm).[65–68] The activation energy of acceptor traps was estimated at ≈100 meV, and concentration $N_A \approx 1.8 \times 10^{18}$ cm^{-3}. Moreover, the structural analysis through XRD confirmed exceptional crystal quality, with a FWHM of 46.8 arcsec for the (020) lattice plane, comparable to the substrate. Raman spectroscopy demonstrated minimal shifts in Raman active phonon modes compared to the substrate, indicating low strain and extended defect levels. EDS showed that the interface does not contain extrinsic impurities. STEM imaging showed no extended defects or dislocations, affirming the high-quality epitaxy. Based on existing knowledge of the native acceptor centers,[28,29,69] collectively, we think that the origin of hole conductivity might be related to V_{Ga}-V_O complex-like defects, strongly enhanced during the growth on (010) substrate.

The important finding in this work is related to the hole mobility, reflecting the nature of free holes. According to the theoretical calculations, self-trapping of holes is expected in many oxides whose valence bands are dominated by O2*p* orbitals, leading to flat valence band. It further leads to a large effective mass which, combined with strong electron–phonon coupling, favors lattice distortion and thus the hole localization, resulting in low hole mobility. At the same time, it should be recalled that a family of *p*-type oxide semiconductors with non-polaronic conduction, i.e., with free holes ($\mu > 1$ cm^2 s^{-1}) are known.[70] **Table 1** summarizes *p*-type oxide semiconductors with free hole mobilities of ≈10 cm^2 V^{-1}·s^{-1} and beyond, including their experimentally reported preparation methods and other electrical transport properties. Indeed, discrepancies between experiments and theoretical predictions for semiconductor oxides, as far as electronic properties are concerned, are not unique in β-Ga$_2$O$_3$.[71,72] For example, in the reference,[73] authors pointed out that early interpretations of small polaron hopping in *p*-type spinel Rh$_2$ZnO$_4$, were based on experimental misinterpretations and limitations of theoretical calculations. Their experiments showed inconsistency with small polaron hopping which were further explained by corrected computational methods, revealing that the self-trapping energy (E_{ST}) is positive, and suggesting the band conduction with heavy, but free, holes in a narrow Rh-t_{2g} valence band.

For β-Ga$_2$O$_3$, theoretical predictions suggested that hole conductivity may have a polaronic character, as holes are expected to be self-trapped.[81–83] However, the EBIC measurements of the diffusion length of minority holes in *n*-type β-Ga$_2$O$_3$,[65–68] along with several other experimental works on Ga$_2$O$_3$//Al$_2$O$_3$ thin films[31,32,34] combined with the present observation of high mobility values, do not match with the small polaronic character of hole conductivity.[84] These experimental findings suggest that holes in β-Ga$_2$O$_3$ may move freely and are not localized. This discrepancy between experimental observations and theoretical predictions, related to the small polaron conduction in β-Ga$_2$O$_3$, highlights the need for further theoretical refinement.

5. Conclusion

In this work, we demonstrated that β-Ga$_2$O$_3$ (010) and (–201) layers simultaneously grown by MOCVD exhibit *p*-type conductivity with pronounced anisotropic electrical transport properties, strongly dependent on the substrate's crystallographic orientation. Our measurements revealed that the (–201) layer has typical *p*-Ga$_2$O$_3$ behavior with deep level defects. At the same time, the hole mobility for this layer ranges from 26 to 36 cm^2 V^{-1}·s^{-1} for the temperatures between 420 and 700 K. The (010) layer, on the other hand, exhibited high free hole concentrations (2.4×10^{17} cm^{-3}) at 370 K with high mobility of 69.4 cm^2 V^{-1}·s^{-1}. High crystalline quality and the absence of extrinsic impurities and extended defects for the layers, grown on the substrates of both orientations, were confirmed by structural and compositional studies.

6. Experimental Section

Sample Preparation: The β-Ga$_2$O$_3$ epilayers were grown simultaneously on β-Ga$_2$O$_3$ (010) and (–201) oriented substrates purchased from Novel Crystal Technology, by horizontal Metal–Organic Chemical Vapor Deposition (MOCVD) set-up. Trimethylgallium (TMGa) and high-purity oxygen were used as the precursors for gallium and oxygen, with 5.5 μmol min^{-1} and 600 sccm flow rates, respectively. Purified argon was used as carrier gas. The pressure and temperature in the growth chamber were maintained at 37 Torr and 775 °C. The thicknesses of (010) and (–201) oriented samples were determined to be ≈1150 and ≈1000 nm, respectively.

X-Ray Diffraction: X-ray diffraction (XRD) data were collected on a 5-circle diffractometer (Rigaku SmartLab) with Cu K$_\alpha$ radiation from a rotating anode. The incident beam was parallelized by a parabolic mirror, reducing the angular divergence to ≈0.01°. Further reduction of the beam divergence was achieved by a channel-cut 2-reflection Ge(220) monochromator, which selected also Cu K$_{\alpha 1}$ radiation. The reflected beam was counted by a NaI scintillation detector. The film roughness was measured by X-ray reflectivity (XRR) and the out-of-plane (OP) orientation and strain by $\theta/2\theta$ scans and rocking curves (ω-scans).

Raman: Raman spectra were recorded using a Renishaw Invia Reflex micro-Raman spectrometer at room temperature. The samples were excited using a cw Modu-Laser Stellar-REN laser emitting at 514.5 nm with a power of 2–4 mW. The reflecting microscope objective was 50× with a NA 0.75; the excitation spot diameter was 1 µm. The back-scattered light was dispersed by a mono chromator with a spectral resolution of 1.4 cm^{-1}. The light was detected by a charge-coupled device. The typical accumulation time was 30 s. Raman shifts were calibrated using an optical phonon frequency (520.5 cm^{-1}) of a silicon monocrystal. Several reference Raman spectra for β-Ga_2O_3 single crystal substrates and sapphire c-cut substrates have been also measured.

AFM: The films surface morphology was investigated using a Bruker Dimension ICON AFM operating in Peak-Force tapping mode. A ScanAsyst Air model tip was used with a 0.4N m^{-1} spring constant and a nominal tip radius of 2 nm. The image resolution was 512 pixels × 512 pixels.

TEM: The crystalline structure of the Ga_2O_3 epilayer was characterized with atomic scale resolution by using high angle annular dark field (HAADF) scanning transmission electron microscopy (STEM, ThermoFisher Spectra microscope operating at 300 kV). The system includes energy dispersive X-ray spectroscopy (EDS) enabling chemical analysis and mapping.

Electrical Measurements: Hall effect measurements were performed in a van der Pauw configuration by custom designed high impedance measurement set-up with magnetic fields of −1.6–1.6 T perpendicular to the film plane. A current source supplies a DC current (2 nA–100 µA) and the exact supplied value is measured with a pico-ammeter. For each switching configuration, monitored with a Keithley 7152 switching system, the adequate statistics is adjusted (typically from 3 to 15) during the measurements. The voltages are recorded using two high impedance Keithley 6517 electrometers and then are subtracted via a Keithley 2700 multimeter. The Hall difference of voltage dynamics is a few tens of microvolts to few tens of volts.

Acknowledgements

The present work is a part of "GALLIA" International Research Project, CNRS, France. GEMaC colleagues acknowledge financial support of French National Agency of Research (ANR), project "GOPOWER", CE-50 N0015-01. The research at UCF was supported in part by NSF (ECCS2310285; ECCS2341747; ECCS 2427262), US-Israel BSF (award # 2022056) and NATO (awards # G6072; G6194). The authors would like to acknowledge Dr. Bernat Mundet for the TEM inspection at ALBA Synchrotron, Dr. José Santiso for the Carine simulations, Dr. Belén Ballesteros, and Dr. Francisco Belarre for the TEM sample preparation at Catalan Institute of Nanoscience and Nanotechnology (ICN2).

Conflict of Interest

The authors declare no conflict of interest.

Data Availability Statement

The data that support the findings of this study are available from the corresponding author upon reasonable request.

Keywords

electrical transport properties, free hole conduction, gallium oxide, p-type, ultra-wide bandgap

Received: March 21, 2025
Revised: August 5, 2025
Published online:

---

[1] E. Chikoidze, T. Tchelidze, C. Sartel, Z. Chi, R. Kabouche, I. Madaci, C. Rubio, H. Mohamed, V. Sallet, F. Medjdoub, A. Perez-Tomas, Y. Dumont, *Mater. Today Phys.* **2020**, *15*, 100263.
[2] J.-S. Li, H.-H. Wan, C.-C. Chiang, T. J. Yoo, M.-H. Yu, F. Ren, H. Kim, Y.-T. Liao, S. J. Pearton, *ECS J. Solid State Sci. Technol.* **2024**, *13*, 035003.
[3] F. Alema, G. Seryogin, A. Osinsky, A. Osinsky, *APL Mater.* **2021**, *9*, 091102.
[4] E. Chikoidze, H. J. von Bardeleben, K. Akaiwa, E. Shigematsu, K. Kaneko, S. Fujita, Y. Dumont, *J. Appl. Phys.* **2016**, *120*, 025109.
[5] Z. Feng, A. F. M. Anhar Uddin Bhuiyan, M. R. Karim, H. Zhao, *Appl. Phys. Lett.* **2019**, *114*, 250601.
[6] K. Goto, K. Konishi, H. Murakami, Y. Kumagai, B. Monemar, M. Higashiwaki, A. Kuramata, S. Yamakoshi, *Thin Solid Films* **2018**, *666*, 182.
[7] W. Zhou, C. Xia, Q. Sai, H. Zhang, *Appl. Phys. Lett.* **2017**, *111*, 242103.
[8] A. K. Rajapitamahuni, A. K. Manjeshwar, A. Kumar, A. Datta, P. Ranga, L. R. Thoutam, S. Krishnamoorthy, U. Singisetti, B. Jalan, *ACS Nano* **2022**, *16*, 8812.
[9] M. Higashiwaki, K. Sasaki, T. Kamimura, M. Hoi Wong, D. Krishnamurthy, A. Kuramata, T. Masui, S. Yamakoshi, *Appl. Phys. Lett.* **2013**, *103*, 123511.
[10] C.-H. Lu, F.-G. Tarntair, Y.-C. Kao, N. Tumilty, R.-H. Horng, *ACS Appl. Electron. Mater.* **2024**, *6*, 568.
[11] W. Li, D. Saraswat, Y. Long, K. Nomoto, D. Jena, H. G. Xing, *Appl. Phys. Lett.* **2020**, *116*, 192101.
[12] J. Zhang, P. Dong, K. Dang, Y. Zhang, Q. Yan, H. Xiang, J. Su, Z. Liu, M. Si, J. Gao, M. Kong, H. Zhou, Y. Hao, *Nat. Commun.* **2022**, *13*, 3900.
[13] F. Zhou, H. Gong, M. Xiao, Y. Ma, Z. Wang, X. Yu, L. Li, L. Fu, H. H. Tan, Y. Yang, F.-F. Ren, S. Gu, Y. Zheng, H. Lu, R. Zhang, Y. Zhang, J. Ye, *Nat. Commun.* **2023**, *14*, 4459.
[14] T. D. Nguyen, Q. Tu, X. Zhang, Y. C. Lin, *Nat. Electron.* **2024**, *7*, 1078.
[15] T. J. Flack, B. N. Pushpakaran, S. B. Bayne, *J. Electron. Mater.* **2016**, *45*, 2673.
[16] A. Ionascut-Nedelcescu, C. Carlone, A. Houdayer, H. J. von Bardeleben, J.-L. Cantin, S. Raymond, *IEEE Trans. Nucl. Sci.* **2002**, *49*, 2733.
[17] A. Kalra, U. U. Muazzam, R. Muralidharan, S. Raghavan, D. N. Nath, *J. Appl. Phys.* **2022**, *131*, 150901.
[18] S. Nakamura, T. M. T. Mukai, M. S. M. Senoh, *Jpn. J. Appl. Phys.* **1991**, *30*, L1998.
[19] S. Onoda, A. Hasuike, Y. Nabeshima, H. Sasaki, K. Yajima, S.-i. Sato, T. Ohshima, *IEEE Trans. Nucl. Sci.* **2013**, *60*, 4446.
[20] D. Kaur, M. Kumar, *Adv. Opt. Mater.* **2021**, *9*, 2002160.
[21] C. Xie, X.-T. Lu, X.-W. Tong, Z.-X. Zhang, F.-X. Liang, L. Liang, L.-B. Luo, Y.-C. Wu, *Adv. Funct. Mater.* **2019**, *29*, 1806006.
[22] J. Xu, W. Zheng, F. Huang, *J. Mater. Chem. C* **2019**, *7*, 8753.
[23] H. Gong, X. Chen, Y. Xu, Y. Chen, F. Ren, B. Liu, S. Gu, R. Zhang, J. Ye, *IEEE Trans. Electron Devices* **2020**, *67*, 3341.
[24] Y. Kokubun, S. Kubo, S. Nakagomi, *Appl. Phys. Express* **2016**, *9*, 091101.
[25] X. Xia, J.-S. Li, C.-C. Chiang, T. J. Yoo, F. Ren, H. Kim, S. J. Pearton, *J. Phys. Appl. Phys.* **2022**, *55*, 385105.
[26] E. Chikoidze, A. Fellous, A. Perez-Tomas, G. Sauthier, T. Tchelidze, C. Ton-That, T. T. Huynh, M. Phillips, S. Russell, M. Jennings, B. Berini, F. Jomard, Y. Dumont, *Mater. Today Phys.* **2017**, *3*, 118.
[27] A. Y. Polyakov, N. B. Smirnov, I. V. Shchemerov, E. B. Yakimov, J. Yang, F. Ren, G. Yang, J. Kim, A. Kuramata, S. J. Pearton, *Appl. Phys. Lett.* **2018**, *112*, 032107.
[28] Z. Chi, C. Sartel, Y. Zheng, S. Modak, L. Chernyak, C. M. Schaefer, J. Padilla, J. Santiso, A. Ruzin, A.-M. Gonçalves, J. von Bardeleben, G. Guillot, Y. Dumont, A. Pérez-Tomás, E. Chikoidze, *J. Alloys Compd.* **2023**, *969*, 172454.
[29] E. Chikoidze, C. Sartel, H. Mohamed, I. Madaci, T. Tchelidze, M. Modreanu, P. Vales-Castro, C. Rubio, C. Arnold, V. Sallet, Y. Dumont, A. Perez-Tomas, *J. Mater. Chem. C* **2019**, *7*, 10231.

[30] E. Serquen, F. Bravo, Z. Chi, L. A. Enrique, K. Lizárraga, C. Sartel, E. Chikoidze, J. A. Guerra, *J. Phys. Appl. Phys.* **2024**, *57*, 495106.

[31] E. Chikoidze, C. Sartel, H. Yamano, Z. Chi, G. Bouchez, F. Jomard, V. Sallet, G. Guillot, K. Boukheddaden, A. Pérez-Tomás, T. Tchelidze, Y. Dumont, *J. Vac. Sci. Technol. A* **2022**, *40*, 043401.

[32] Z. Y. Wu, Z. X. Jiang, C. C. Ma, W. Ruan, Y. Chen, H. Zhang, G. Q. Zhang, Z. L. Fang, J. Y. Kang, T.-Y. Zhang, *Mater. Today Phys.* **2021**, *17*, 100356.

[33] Z. Chi, S.-R. Park, L. Burdiladze, T. Tchelidze, J.-M. Chauveau, Y. Dumont, S.-M. Koo, Z. Kushitashvili, A. Bibilashvili, G. Guillot, A. Pérez-Tomás, X.-Y. Tsai, F.-G. Tarntair, R. H. Horng, E. Chikoidze, *Mater. Today Phys.* **2024**, *49*, 101602.

[34] R. H. Horng, X.-Y. Tsai, F.-G. Tarntair, J.-M. Shieh, S.-H. Hsu, J. P. Singh, G.-C. Su, P.-L. Liu, *Mater. Today Adv.* **2023**, *20*, 100436.

[35] C.-Y. Huang, X.-Y. Tsai, F.-G. Tarntair, C. Langpoklakpam, T. S. Ngo, P.-J. Wang, Y.-C. Kao, Y.-K. Hsiao, N. Tumilty, H.-C. Kuo, T.-L. Wu, C.-L. Hsiao, R.-H. Horng, *Mater. Today Adv.* **2024**, *22*, 100499.

[36] C. Liu, Z. Wu, H. Zhai, J. Hoo, S. Guo, J. Wan, J. Kang, J. Chu, Z. Fang, *J. Mater. Sci. Technol.* **2025**, *209*, 196.

[37] H. Zhai, C. Liu, Z. Wu, C. Ma, P. Tian, J. Wan, J. Kang, J. Chu, Z. Fang, *Sci. China Mater.* **2024**, *67*, 898.

[38] Y. Zhao, Z. Wu, C. Liu, X. Yue, J. Chen, C. Cong, J. Wang, J. Kang, J. Chu, Z. Fang, *Mater. Today Phys.* **2024**, *44*, 101447.

[39] Q. Li, B.-D. Du, J.-Y. Gao, J. Liu, *Appl. Phys. Rev.* **2023**, *10*, 011402.

[40] F. Alema, T. Itoh, W. Brand, A. Osinsky, J. S. Speck, *Appl. Phys. Lett.* **2023**, *122*, 252105.

[41] D. Gogova, D. Q. Tran, V. Stanishev, V. Jokubavicius, L. Vines, M. Schubert, R. Yakimova, P. P. Paskov, V. Darakchieva, *J. Vac. Sci. Technol. A* **2024**, *42*, 022708.

[42] L. Meng, D. Yu, H.-L. Huang, C. Chae, J. Hwang, H. Zhao, *Cryst. Growth Des.* **2024**, *24*, 3737.

[43] S. B. Anooz, R. Grüneberg, T.-S. Chou, A. Fiedler, K. Irmscher, C. Wouters, R. Schewski, M. Albrecht, Z. Galazka, W. Miller, J. Schwarzkopf, A. Popp, *J. Phys. Appl. Phys.* **2020**, *54*, 034003.

[44] J. Cooke, P. Ranga, A. Bhattacharyya, X. Cheng, Y. Wang, S. Krishnamoorthy, M. A. Scarpulla, B. Sensale-Rodriguez, *J. Vac. Sci. Technol. A* **2022**, *41*, 013406.

[45] R. Schewski, K. Lion, A. Fiedler, C. Wouters, A. Popp, S. V. Levchenko, T. Schulz, M. Schmidbauer, S. Bin Anooz, R. Grüneberg, Z. Galazka, G. Wagner, K. Irmscher, M. Scheffler, C. Draxl, M. Albrecht, *APL Mater.* **2018**, *7*, 022515.

[46] S. Rafique, M. R. Karim, J. M. Johnson, J. Hwang, H. Zhao, *Appl. Phys. Lett.* **2018**, *112*, 052104.

[47] K. Goto, H. Murakami, A. Kuramata, S. Yamakoshi, M. Higashiwaki, Y. Kumagai, *Appl. Phys. Lett.* **2022**, *120*, 102102.

[48] H. Murakami, K. Nomura, K. Goto, K. Sasaki, K. Kawara, Q. T. Thieu, R. Togashi, Y. Kumagai, M. Higashiwaki, A. Kuramata, S. Yamakoshi, B. Monemar, A. Koukitu, *Appl. Phys. Express* **2014**, *8*, 015503.

[49] P. Mazzolini, A. Falkenstein, C. Wouters, R. Schewski, T. Markurt, Z. Galazka, M. Martin, M. Albrecht, O. Bierwagen, *APL Mater.* **2020**, *8*, 011107.

[50] K. Ghosh, U. Singisetti, *J. Appl. Phys.* **2017**, *122*, 035702.

[51] C. Ma, Z. Wu, Z. Jiang, Y. Chen, W. Ruan, H. Zhang, H. Zhu, G. Zhang, J. Kang, T.-Y. Zhang, J. Chu, Z. Fang, *J. Mater. Chem. C* **2022**, *10*, 6673.

[52] N. Ma, N. Tanen, A. Verma, Z. Guo, T. Luo, H. (Grace) Xing, D. Jena, *Appl. Phys. Lett.* **2016**, *109*, 212101.

[53] K. Sasaki, M. Higashiwaki, A. Kuramata, T. Masui, S. Yamakoshi, *J. Cryst. Growth* **2014**, *392*, 30.

[54] K. Ikenaga, N. Tanaka, T. Nishimura, H. Iino, K. Goto, M. Ishikawa, H. Machida, T. Ueno, Y. Kumagai, *J. Cryst. Growth* **2022**, *582*, 126520.

[55] D. Dohy, G. Lucazeau, A. Revcolevschi, *J. Solid State Chem.* **1982**, *45*, 180.

[56] D. Machon, P. F. McMillan, B. Xu, J. Dong, *Phys. Rev. B* **2006**, *73*, 094125.

[57] S. Zhang, J. Wang, Z. Li, R. Zhao, L. Tong, Z. Liu, J. Zhang, Z. Liu, *J. Phys. Chem. C* **2016**, *120*, 10605.

[58] S. Kumar, G. Sarau, C. Tessarek, M. Y. Bashouti, A. Hähnel, S. Christiansen, R. Singh, *J. Phys. Appl. Phys.* **2014**, *47*, 435101.

[59] C. Kranert, C. Sturm, R. Schmidt-Grund, M. Grundmann, *Sci. Rep.* **2016**, *6*, 35964.

[60] J. M. Johnson, Z. Chen, J. B. Varley, C. M. Jackson, E. Farzana, Z. Zhang, A. R. Arehart, H.-L. Huang, A. Genc, S. A. Ringel, C. G. Van de Walle, D. A. Muller, J. Hwang, *Phys. Rev. X* **2019**, *9*, 041027.

[61] A. F. M. Anhar Uddin Bhuiyan, Z. Feng, J. M. Johnson, Z. Chen, H.-L. Huang, J. Hwang, H. Zhao, *Appl. Phys. Lett.* **2019**, *115*, 120602.

[62] T. Yoo, X. Xia, F. Ren, A. Jacobs, M. J. Tadjer, S. Pearton, H. Kim, *Appl. Phys. Lett.* **2022**, *121*, 072111.

[63] S. Jang, S. Jung, K. Beers, J. Yang, F. Ren, A. Kuramata, S. J. Pearton, K. H. Baik, *J. Alloys Compd.* **2018**, *731*, 118.

[64] L. Chernyak, S. Lovo, J.-S. Li, C.-C. Chiang, F. Ren, S. J. Pearton, C. Sartel, Z. Chi, Y. Dumont, E. Chikoidze, A. Schulte, A. Ruzin, U. Shimanovich, *AIP Adv.* **2024**, *14*, 115301.

[65] J. Lee, E. Flitsiyan, L. Chernyak, J. Yang, F. Ren, S. J. Pearton, B. Meyler, Y. J. Salzman, *Appl. Phys. Lett.* **2018**, *112*, 082104.

[66] S. Modak, J. Lee, L. Chernyak, J. Yang, F. Ren, S. J. Pearton, S. Khodorov, I. Lubomirsky, *AIP Adv.* **2019**, *9*, 015127.

[67] A. Y. Polyakov, E. B. Yakimov, D. S. Saranin, A. V. Chernykh, A. A. Vasilev, P. Gostishchev, A. I. Kochkova, L. A. Alexanyan, N. R. Matros, I. V. Shchemerov, S. J. Pearton, *J. Appl. Phys.* **2024**, *135*, 165703.

[68] E. B. Yakimov, A. Y. Polyakov, N. B. Smirnov, I. V. Shchemerov, J. Yang, F. Ren, G. Yang, J. Kim, S. J. Pearton, *J. Appl. Phys.* **2018**, *123*, 185704.

[69] A. Usseinov, A. Platonenko, Z. Koishybayeva, A. Akilbekov, M. Zdorovets, A. I. Popov, *Opt. Mater. X* **2022**, *16*, 100200.

[70] K. H. L. Zhang, K. Xi, M. G. Blamire, R. G. Egdell, *J. Phys. Condens. Matter* **2016**, *28*, 383002.

[71] A. Ohtomo, H. Y. Hwang, *Nature* **2004**, *427*, 423.

[72] F. Tran, P. Blaha, *Phys. Rev. Lett.* **2009**, *102*, 226401.

[73] A. R. Nagaraja, N. H. Perry, T. O. Mason, Y. Tang, M. Grayson, T. R. Paudel, S. Lany, A. Zunger, *J. Am. Ceram. Soc.* **2012**, *95*, 269.

[74] S. J. Lee, Y. Jang, H. J. Kim, E. S. Hwang, S. M. Jeon, J. S. Kim, T. Moon, K.-T. Jang, Y.-C. Joo, D.-Y. Cho, C. S. Hwang, *ACS Appl. Mater. Interfaces* **2018**, *10*, 3810.

[75] J. A. Caraveo-Frescas, P. K. Nayak, H. A. Al-Jawhari, D. B. Granato, U. Schwingenschlögl, H. N. Alshareef, *ACS Nano* **2013**, *7*, 5160.

[76] H. Kawazoe, M. Yasukawa, H. Hyodo, M. Kurita, H. Yanagi, H. Hosono, *Nature* **1997**, *389*, 939.

[77] K. Zhang, V. G. T. Vangipuram, H.-L. Huang, J. Hwang, H. Zhao, *Adv. Electron. Mater.* **2023**, *11*, 2300550.

[78] A. Bhatia, G. Hautier, T. Nilgianskul, A. Miglio, J. Sun, H. J. Kim, K. H. Kim, S. Chen, G.-M. Rignanese, X. Gonze, J. Suntivich, *Chem. Mater.* **2016**, *28*, 30.

[79] K. Matsuzaki, K. Nomura, H. Yanagi, T. Kamiya, M. Hirano, H. Hosono, *Appl. Phys. Lett.* **2008**, *93*, 202107.

[80] B. S. Li, K. Akimoto, A. Shen, *J. Cryst. Growth* **2009**, *311*, 1102.

[81] P. Deák, Q. D. Ho, F. Seemann, B. Aradi, M. Lorke, T. Frauenheim, *Phys. Rev. B* **2017**, *95*, 075208.

[82] B. E. Kananen, L. E. Halliburton, K. T. Stevens, G. K. Foundos, N. C. Giles, *Appl. Phys. Lett.* **2017**, *110*, 202104.

[83] J. B. Varley, A. Janotti, C. Franchini, C. G. Van de Walle, *Phys. Rev. B* **2012**, *85*, 081109.

[84] C. Franchini, M. Reticcioli, M. Setvin, U. Diebold, *Nat. Rev. Mater.* **2021**, *6*, 560.